

---

This manuscript has been accepted for publication in the *Journal of Nuclear Materials*. Please note that, despite having undergone peer-review, the manuscript has yet to be formally published. Printed version may have slightly different content. The final version of this manuscript will be available via the ‘Peer-reviewed Publication DOI’ link. Please feel free to contact the corresponding author. Any feedback will be greatly appreciated.

---

1 **Effect of solution chemistry on the iodine release from iodoapatite in aqueous environments**

2 Zelong Zhang <sup>†\*</sup>, Léa Gustin<sup>‡1</sup>, Weiwei Xie<sup>‡</sup>, Jie Lian<sup>§</sup>, Kalliat T. Valsaraj<sup>||</sup>, and Jianwei Wang<sup>†,⊥</sup>

3 <sup>†</sup> Department of Geology and Geophysics, Louisiana State University, Baton Rouge, Louisiana  
4 70803 United States

5 <sup>‡</sup> Department of Chemistry, Louisiana State University, Baton Rouge, Louisiana 70803 United  
6 States

7 <sup>§</sup> Department of Mechanical, Aerospace, and Nuclear Engineering, Rensselaer Polytechnic  
8 Institute, 110 Eighth Street, Troy, New York 12180, United States

9 <sup>||</sup> Cain Department of Chemical Engineering, Louisiana State University, Baton Rouge,  
10 Louisiana 70803 United States

11 <sup>⊥</sup> Center for Computation and Technology, Louisiana State University, Baton Rouge, Louisiana  
12 70803, United States

13 \*Corresponding to zelongz@lsu.edu

14

---

<sup>1</sup> Current address: Department of Chemistry, University of Wisconsin-Madison, Madison, Wisconsin 53706, United States

15 **Highlights**

- 16 • First study on the effect of aqueous ions on the degradation of waste form for I-129
- 17 • First summary on probable iodine release pathways in various aqueous environments
- 18 • Accelerated iodine release by enhanced ion-exchange, basic pH, and ionic strength
- 19 • Discovered secondary phase vanadinite  $Pb_5(VO_4)_3Cl$  and hydroxylvanadinite
- 20  $Pb_5(VO_4)_3OH$
- 21 • Low ionic content and neutral pH are vital to the disposal safety of nuclear waste

22

23 **Abstract**

24 To ensure the safe disposal of nuclear waste, understanding the release process of radionuclides  
25 retained in the nuclear waste forms is of vital importance. Iodoapatite  $\text{Pb}_{9.85}(\text{VO}_4)_6\text{I}_{1.7}$ , a potential  
26 waste form for iodine-129, was selected as a model system for ceramic waste forms in this study  
27 to understand the effect of aqueous species on iodine release. Semi-dynamic leaching tests were  
28 conducted on bulk samples in cap-sealed Teflon vessels with 0.1 mol/L NaCl,  $\text{Na}_2\text{CO}_3$ ,  $\text{Na}_3\text{PO}_4$ ,  
29 and  $\text{Na}_2\text{SO}_4$  solutions under 90 °C, fixed sample surface area to solution volume ratio of 5/m,  
30 and periodic replacement of leaching solutions. The reacted solutions were then analyzed by  
31 Inductively Coupled Plasma-Mass Spectrometry and Inductively Coupled Plasma-Optical  
32 Emission Spectrometry; the leached surfaces were characterized by X-ray diffraction, scanning  
33 electron microscopy, and infrared spectroscopy. The result shows that, compared to deionized  
34 water, the ion-rich solutions enhanced the iodine release as a result of the increased ionic  
35 strength, reduced activity coefficient of dissolved species, and increased solution pH. Surface  
36 reactions can lead to the formations of secondary phases by ion-exchange and precipitation.  
37 These findings suggest that an ion-rich environment in the geological repository can be  
38 detrimental to the disposal safety of the nuclear waste form.

## 39 **1 Introduction**

40 Nuclear energy is emission-free. The deployment of nuclear energy is motivated by the  
41 pressing demand to mitigate climate change.<sup>1</sup> Sustainable development of the nuclear energy  
42 requires concrete plans to safely dispose radionuclides waste generated by nuclear fission.<sup>2</sup>  
43 Among those radionuclides, iodine-129 is particularly challenging to handle due to its long half-  
44 life (15.7 million years), high yield (0.7% yield per fission of uranium-235),<sup>3</sup> and weak  
45 interactions with common materials in repository environments such as engineering barrier and  
46 rock in geology formation.<sup>4,5</sup> Iodide ( $I^-$ ) is the most stable form of iodine in an environment with  
47 pH and redox potential typically found in nature.<sup>6-8</sup> Under highly oxidizing conditions, iodide  
48 can be oxidized to iodine ( $I_2$ ) and/or iodate ( $IO_3^-$ ). All these iodine species are highly mobile in  
49 nature given their high volatility and or high solubility.<sup>9,10</sup> Iodine, as an essential element for  
50 human health, can accumulate in human bodies.<sup>11</sup> For a healthy adult, 30% of the total iodine,  
51 approximately 15-20 mg, is concentrated in the thyroid gland.<sup>12</sup> Chronical radiation from iodine-  
52 129 beta decay can induce cancer to the thyroid follicular cells.<sup>11</sup> Therefore, iodine-129 is a  
53 primary contributor of the radiation dosage when analyzing the safety of disposal environments.<sup>4</sup>  
54 The immobilization of iodine-129 is one of the critical research subjects for nuclear waste  
55 management.<sup>4,13-18</sup>

56 The most probable scenarios that compromise nuclear waste forms in a repository  
57 environment are the contact with aqueous solutions.<sup>19,20</sup> In a typical repository, nuclear waste  
58 forms are packed into corrosion resistant metallic canisters underground.<sup>21</sup> Canister corrosion  
59 and degradation are anticipated to be the result of corrodents carried by groundwater.<sup>22</sup> Through  
60 infiltration and percolation of precipitation and groundwater aquifer, water can reach the  
61 canisters and supply corrodents to react with the canister material. Upon the breaching of the

62 canister, the waste forms are exposed to an aqueous environment. Owing to the long half-life of  
63 iodine-129, it is crucial to predict the long-term chemical durability of iodine waste forms. To  
64 enable such prediction, it is necessary to obtain a fundamental understanding of corrosion  
65 mechanisms of waste forms and how iodine in the host material is released in various solutions  
66 that may occur under repository conditions.

67 Several waste form materials including glass, ceramics, glass-ceramics, cement, and  
68 composite have been proposed to immobilize iodine.<sup>18,23</sup> These waste forms immobilize iodine  
69 via two major mechanisms: encapsulation and incorporation. To encapsulate iodine, the host  
70 matrices need to contain iodine in a designated phase different from the host material. One  
71 example is zeolite structure, in which iodine-bearing phases can be adsorbed on zeolite's  
72 framework.<sup>17,24</sup> Iodine can also be incorporated as a compositional element into the host matrix  
73 structure through chemical bonding, such as iodoapatite  $Pb_5(VO_4)_3I$  and sodalite  
74  $Na_4(AlSiO_4)_3I$ .<sup>13,25-27</sup>

75 The difficulty to study the durability of different waste forms varies on a case-by-case basis.  
76 It is particularly challenging to evaluate the encapsulation waste forms due to the complexity of  
77 multi-phase and microstructures. On the other hand, characterizing the corrosion mechanism can  
78 be relatively straightforward for single-phase crystal waste forms which have well-defined  
79 crystal structures and simple microstructures. Based on the simplicity of its crystal structure and  
80 microstructure, iodoapatite is chosen in this study as the model system of ceramic waste forms  
81 that can incorporate radionuclides. In addition, apatite ceramics is a promising material due to its  
82 thermal, mechanical, and chemical stability.<sup>13,25,28,29</sup> These advantages are also demonstrated in  
83 nature as apatite has been found as a retention matrix for actinides and fission products in natural  
84 fission reactors at Franceville basin in Africa.<sup>22,30</sup>

85 Several chemical durability tests have been performed on single-phase crystal waste forms.  
86 Uno et al. in 2001 conducted soxhlet leach method on apatite  $\text{Pb}_{10}(\text{VO}_4)_6\text{I}_2$ .<sup>31</sup> Soxhlet leach  
87 method is designed to maximize the number of leachable constituents in leachant by allowing a  
88 continuous contact between the waste and recycling leachant in a closed system.<sup>32</sup> The iodine  
89 release rate,  $3.98 \times 10^{-5} \text{ g} \cdot \text{cm}^{-2} \cdot \text{d}^{-1}$ , was reported.<sup>31</sup> Guy et al. in 2002 studied apatite  
90  $\text{Pb}_{10}(\text{VO}_4)_{4.8}(\text{PO}_4)_{1.2}\text{I}_2$  dissolution in aqueous solutions.<sup>33</sup> The resulting data shows that iodine  
91 release was incongruent and exhibited dependency on temperature and pH. They also discovered  
92 a secondary phase, lead vanado-phosphate, precipitated at the sample surface. Zhang et al. in  
93 2007 performed static leaching test on  $\text{Pb}_5(\text{VO}_4)_3\text{I}$  powder in a basic  $\text{KOH}/\text{KHCO}_3$  buffer  
94 solution.<sup>34</sup> Spectroscopic evidences show that  $\text{OH}^-$  and  $\text{CO}_3^{2-}$  can substitute  $\text{I}^-$  and  $\text{VO}_4^{3-}$  in  
95 apatite. Maddrell et al. in 2014 conducted static leach tests on crushed powder iodide sodalite  
96  $\text{Na}_4(\text{AlSiO}_4)_3\text{I}$  in  $\text{KOH}/\text{KHCO}_3$  buffer solutions.<sup>26</sup> The result suggests a congruent dissolution.<sup>26</sup>  
97 Three leaching static experiments with durations of 3, 7, and 14 days exhibited a logarithmic  
98 increase of iodine release. More recently, in 2017 Coulon et al. applied static leaching technique  
99 to study the iodate-substituted hydroxyapatite in deionized water and groundwater.<sup>35</sup> They  
100 reported that the iodine release is controlled by congruent dissolution under unsaturated  
101 conditions and controlled by diffusion through ion exchange under saturated condition.  
102 Interestingly, when groundwater was used as leachant, secondary phase hydroxyapatite  
103 precipitated on the sample surface. Based on these studies, static leach test is a preferable method  
104 to study the waste form durability due to the following reasons: 1) its simple procedure can  
105 accommodate a wide range of test conditions; 2) the resultant data can be used to interpret the  
106 release mechanism.<sup>36</sup> Static leaching method assumes that the solution feedback is negligible,  
107 which is valid under conditions of sufficiently low surface to volume ratio.<sup>36</sup> However, the

108 solution feedback can gradually increase over time in a static leaching experiment. In cases  
109 where the solution is oversaturated for phases of low solubility, secondary phases can precipitate  
110 at the leached surface. Therefore, it can be problematic to use data from static leaching tests to  
111 predict waste form behavior in a repository environment.<sup>37</sup> To address the issues of solution  
112 feedback, a semi-dynamic leaching method was implemented by Zhang et al. in 2018 to quantify  
113 the processes involved in the iodine release of an iodine-bearing apatite.<sup>29</sup> In their experiment,  
114 deionized water solutions, as the leachant, were replaced periodically to minimize the solution  
115 feedback. They demonstrated that iodine released from apatite is driven by short-term diffusion  
116 and long-term matrix dissolution. This semi-dynamic approach was employed to produce  
117 essential datasets to parameterize a mechanistic model suitable for predicting the kinetics of  
118 iodine release under different conditions.<sup>37</sup>

119 Since the aqueous systems in natural environment contain a variety of dissolved species, it is  
120 necessary to understand how these aqueous species affect the iodine release from iodine waste  
121 forms in an aqueous environment. For instance, the iodine release from apatite structured  
122 materials can be enhanced by rapid substitution of halogen element<sup>38-41</sup> or inhibited by  
123 precipitation of secondary phase.<sup>33,35,37</sup> In this study, we conducted semi-dynamic leach tests on  
124 single phase crystal ceramics of iodoapatite in 0.1 mol/L NaCl, Na<sub>2</sub>CO<sub>3</sub>, Na<sub>3</sub>PO<sub>4</sub> and Na<sub>2</sub>SO<sub>4</sub>  
125 solutions. The goal is to examine the impact of the solution chemistry on the kinetics of  
126 iodoapatite dissolution. We hypothesized that dissolved aqueous species, via ion exchange and  
127 precipitation, can substantially impact the dissolution kinetics; this effect should highly depend  
128 on the chemistry of the aqueous species and the surface reactions of specific phases. The finding  
129 of this study is expected to provide important insight into the long-term performance of iodine  
130 waste forms and guidance to improve the disposal safety of nuclear waste.



## 131 **2 Experimental**

### 132 **2.1 Materials and methods**

133 Our samples, obtained from previous studies,<sup>25</sup> were dense ceramic chips in  
134 quadrilateral shape: 4.7 – 10.3 millimeter long by 1.1 – 1.8 millimeter thick with a  
135 chemical composition of  $\text{Pb}_{9.85}(\text{VO}_4)_6\text{I}_{1.7}$  according to the EDS and X-ray diffraction  
136 refinement, as shown in Figs. 1, 2 and 4. The iodoapatite samples were synthesized by  
137 using high energy ball milling (HEBM) and spark plasma sintering (SPS) techniques.  
138 Sample surfaces were polished by 4000-grit sandpaper on a mechanical polishing wheel  
139 lubricated with ethanol. Details of the synthesis and characterization of these samples  
140 were reported previously in separate publications.<sup>25,29,37</sup>

141 The leaching method was adopted from ASTM C1308 standard test, as described in  
142 the previous study<sup>29,37</sup>. Four parallel experiments were conducted simultaneously for 14  
143 days in four different leaching solutions: 0.1 mol/L NaCl, 0.1 mol/L  $\text{Na}_2\text{CO}_3$ , 0.1 mol/L  
144  $\text{Na}_3\text{PO}_4$ , and 0.1 mol/L  $\text{Na}_2\text{SO}_4$ . Sample surface area ( $\text{m}^2$ ) to solution volume ( $\text{m}^3$ ) ratios  
145 (S/V) of all four tests were fixed and maintained at 5/m. The leached solutions were  
146 replaced every 24 hours. All reactor vessels were weighed before and after each interval  
147 to monitor the solution losses which were within 0.5 % of the initial solution mass. In  
148 addition, a control test was conducted in deionized water under identical conditions for 7  
149 days using the same protocol. All samples after leaching experiments were collected,  
150 rinsed by deionized water and ethanol, and air-dried.

### 151 **2.2 Characterization**

152 The elements of interest in the leachate solutions are I, Pb, and V. The leached  
153 solutions, depending on the solution chemistry, were analyzed by Inductively Coupled  
154 Plasma-Mass Spectrometry (ICP-MS, PerkinElmer Elan 9000) and/or Inductively-  
155 Coupled Plasma-Optical Emission Spectrometry (ICP-OES, SPECTRO Ametek Spectro  
156 ARCOS). Two standard solutions from Inorganic Ventures were used in the solution  
157 analysis: 1)  $1.001 \pm 0.007 \mu\text{g}/\text{mL}$  iodide in  $\text{H}_2\text{O}$  solution and 2)  $1.000 \pm 0.007 \mu\text{g}/\text{mL}$   
158 lead and  $1.000 \pm 0.006 \mu\text{g}/\text{mL}$  vanadium in 1%  $\text{HNO}_3$  solution. Chemical properties of  
159 solution at equilibrium state such as pH, ionic strength, speciation, and activity were  
160 calculated by Visual MINTEQ package.

161 Samples were characterized by Scanning Electron Microscopy (SEM), Infrared  
162 spectroscopy (IR), and X-ray diffraction spectroscopy (XRD). SEM images were taken by  
163 a FEI Quanta SEM system with FEI Versa 3D DualBeam. Infrared spectroscopy was  
164 performed on a Thermo Nicolet Continuum Infrared Microscope under Specular  
165 Reflection mode and transmission mode with a fixed incident angle and an aperture area  
166 of 10 by 10  $\mu\text{m}$  covering 4000 to 650  $\text{cm}^{-1}$  at a spectral resolution of 2  $\text{cm}^{-1}$ . XRD data  
167 were collected from PANalytical Empyrean X-Ray Diffractometer equipped with  
168 monochromated  $\text{Cu-K}\alpha$  radiation ( $\lambda = 1.5406 \text{ \AA}$ ), operated at 45 kV, 40 mA, a step size of  
169  $0.026^\circ$ , and a scanning range from 5 to  $100^\circ$ .

170 The crystal structures were refined by Le Bail algorithm using Jana2006 program.<sup>42</sup>  
171 All parameters were refined by the least-squares method. The pseudo-Voigt function was  
172 used as the peak profile function. Structural parameters of  $\text{Pb}_{9.85}(\text{VO}_4)_6\text{I}_{1.7}$  measured by  
173 Audubert et al. were used as initial input (hexagonal, space group P63/m,  $a = b = 10.422$   
174  $\text{\AA}$ ,  $c = 7.467 \text{ \AA}$ ,  $\alpha = \beta = 90^\circ$ ;  $\gamma = 120^\circ$ ).<sup>43</sup>

## 175 **3 Results**

### 176 **3.1 Leached surface characterization by SEM/EDS**

177 In Fig. 1 (a-c), no changes observable by naked eyes occurred on the surfaces of  
178 samples leached by NaCl and NaSO<sub>4</sub> solutions for 14 days, whereas white layers were  
179 gradually formed on the sample surfaces leached by Na<sub>2</sub>CO<sub>3</sub> and Na<sub>3</sub>PO<sub>4</sub> solutions within  
180 the first week of the experiments. The SEM images in Fig. 1 (d-i) show that the surface  
181 alterations on samples leached by NaCl and Na<sub>2</sub>SO<sub>4</sub> solutions were moderate, similar to  
182 the water leached surface. However, samples leached by Na<sub>2</sub>CO<sub>3</sub> and Na<sub>3</sub>PO<sub>4</sub> solutions  
183 demonstrated significant surface corrosion and possible formation of new phases. The  
184 surface leached by Na<sub>2</sub>CO<sub>3</sub> exhibited large grains, while congregated structures of similar  
185 size appeared on the surface leached by Na<sub>3</sub>PO<sub>4</sub>.

186 According to EDS analysis, the surface chemical compositions in Fig. 2 indicate  
187 considerable changes between the leached samples and the pristine one. The key features  
188 of EDS spectrum of pristine iodoapatite are: a carbon peak at 0.3 keV from background  
189 (carbon tape), an oxygen peak at 0.5 keV, a broad Pb band from 2.34 to 2.45 keV  
190 shouldered with two small Pb peaks at 1.8 and 2.6 keV, three iodine peaks at 3.9, 4.2, and  
191 4.5 keV, and vanadium peaks at 4.9 and 5.4 keV. Overall, the iodine peaks at 3.94 keV  
192 are nearly diminished in the EDS spectra of all four leached surfaces. The samples  
193 leached by NaCl and Na<sub>3</sub>PO<sub>4</sub> exhibited a substantial amount of chloride and phosphorus  
194 signals at 2.62 and 2.01 keV, respectively. On the sample leached by NaCl, the Pb peak at  
195 2.62 keV is comparable to the Pb peak at 1.8 keV, while the 2.62 keV peaks of the rest  
196 samples are much weaker than their corresponding 1.8 keV peaks. Carbon signal at 0.27

197 keV from Na<sub>2</sub>CO<sub>3</sub> leached sample cannot be properly quantified due to the background  
198 interference from carbon tape and the graphite impurity introduced during sample  
199 synthesis. Sulfur EDS peak at 2.31 keV overlaps with the broad central peak of Pb at 2.34  
200 keV. Na<sub>2</sub>SO<sub>4</sub> leached surface exhibited no sulfur peak near 2.3 keV given the  
201 resemblance of the band shape between the sample leached by Na<sub>2</sub>SO<sub>4</sub> and the rest. We  
202 noticed variations of carbon and oxygen EDS signals among these samples which were  
203 induced by the instrumentation settings such as sample orientation and beam parameters.  
204 Therefore, carbon and oxygen were not considered in the EDS analysis.

### 205 **3.2 Leached surface characterization by IR analysis**

206 The IR spectroscopy results are listed in Fig. 3. All these four samples yielded two  
207 main peaks near 750 and 890 cm<sup>-1</sup>, which are attributed to V-O bond.<sup>34</sup> Pristine  
208 iodoapatite and samples leached by water, Na<sub>2</sub>SO<sub>4</sub>, and NaCl showed nearly identical  
209 spectra. Surfaces leached by Na<sub>2</sub>CO<sub>3</sub> and Na<sub>3</sub>PO<sub>4</sub> exhibited position shifts of these two  
210 V-O peaks to the region of 700 to 900 cm<sup>-1</sup> and multiple new bands. Sample leached by  
211 Na<sub>2</sub>CO<sub>3</sub> yielded sharp bands near 785, 890, 960, 1200, and 1450 cm<sup>-1</sup>, in which the broad  
212 band at 1450 cm<sup>-1</sup> is attributed to the stretching vibration of CO<sub>3</sub><sup>2-</sup>.<sup>44,45</sup> The Na<sub>3</sub>PO<sub>4</sub>  
213 leached surface generated IR peaks near 785, 870, 950, 1110, 1420, 1800, and 2200 cm<sup>-1</sup>,  
214 in which some can be assigned to the PO<sub>4</sub><sup>3-</sup> (e.g. ν<sub>1</sub> – 950 cm<sup>-1</sup>, ν<sub>3</sub> – 1100 cm<sup>-1</sup>).<sup>44</sup>  
215 Interestingly, both CO<sub>3</sub><sup>2-</sup> and PO<sub>4</sub><sup>3-</sup> leached surfaces showed visible OH<sup>-</sup> stretching  
216 vibration near 3500 cm<sup>-1</sup>,<sup>34,44</sup> which also occurred on water leached surface under IR  
217 transmission mode.<sup>29</sup>

### 218 **3.3 Leached surface characterization by XRD**

219 The XRD data are shown in Fig. 4. All these leached samples demonstrated  
220 substantial differences compared to the pristine sample. Based on the XRD pattern, these  
221 leached samples can be categorized into two groups: I) surfaces leached by NaCl and  
222 Na<sub>2</sub>SO<sub>4</sub> solutions, the pristine, and water leached sample; II) surfaces leached by Na<sub>2</sub>CO<sub>3</sub>  
223 and Na<sub>3</sub>PO<sub>4</sub> solutions, which were similar to the standard hydroxylvanadinite. The XRD  
224 patterns of Group I are alike, which indicates no substantial structural changes compared  
225 to the pristine. The XRD patterns of Group II display enhanced peak splitting between  
226 25° and 28°. The original peak splitting of the pristine sample reflects the apatite structure  
227 deformation which accommodates the relatively large iodide incorporated in the apatite  
228 framework. The peak splitting of Na<sub>2</sub>SO<sub>4</sub> leached surface is slightly enhanced, compared  
229 to the pristine, but is weaker than the water leached sample. Interestingly, NaCl leached  
230 surface yielded a diminished splitting at 26° and a new peak occurred at 29°, later  
231 identified as  $1\bar{3}1$  shown in Fig. 5. The Full Width at Half Maximum (FWHM) of XRD  
232 from NaCl leached surface was considerably broadened to ~0.4° compared to ~0.2° from  
233 other samples, which may be attributed to the peak overlapping resulting from the  
234 presence of a secondary phase. Both Na<sub>2</sub>CO<sub>3</sub> and Na<sub>3</sub>PO<sub>4</sub> leached samples exhibited  
235 nearly identical XRD pattern, resembling the pattern of standard hydroxylvanadinite  
236 Pb<sub>10</sub>(VO<sub>4</sub>)<sub>6</sub>(OH)<sub>2</sub>. The two highest bands on Pb<sub>10</sub>(VO<sub>4</sub>)<sub>6</sub>(OH)<sub>2</sub> standard are 112 and  $1\bar{3}1$   
237 with an order of intensity  $I_{112} < I_{1\bar{3}1}$ . Same bands 112 and  $1\bar{3}1$  also have the highest  
238 intensity on Na<sub>2</sub>CO<sub>3</sub> and Na<sub>3</sub>PO<sub>4</sub> leached samples, however, the intensity of 112 is higher  
239 than that of  $1\bar{3}1$ ,  $I_{112} > I_{1\bar{3}1}$ .

240 The Le Bail method was applied to obtain structural information from the XRD data.  
241 Table 1 compares the refined lattice parameters between sample surfaces of different

242 conditions and standards. No noticeable changes occurred in the crystal structures of  
243 samples leached by deionized water and Na<sub>2</sub>SO<sub>4</sub> when compared to that of pristine  
244 sample (their length of *a*-, *b*-, and *c*-axes are approximately ~10.4, ~10.4, and ~7.5 Å,  
245 respectively). On the other hand, a ~0.2 Å contraction along both the *a*- and *b*-axes were  
246 observed for the samples leached by Na<sub>2</sub>CO<sub>3</sub> and Na<sub>3</sub>PO<sub>4</sub> solutions while the *c*-axis  
247 remains the same and is consistent with other samples at ~7.45 Å. The observed and  
248 calculated diffraction patterns, the residual and the indices of the main reflections of NaCl  
249 leached sample are shown in Fig. 5. We identified a secondary phase vanadinite  
250 Pb<sub>5</sub>(VO<sub>4</sub>)<sub>3</sub>Cl, indicating the substitution of iodine by chlorine during NaCl leaching.

### 251 **3.4 Solution composition analysis by ICP-MS and ICP-OES**

252 The results of the solution analysis on the leachates collected from the leach tests are  
253 shown in Fig. 6. The release rates of iodine, lead, and vanadium are depicted as green  
254 circles, blue squares, and red triangles, respectively. In Fig. 6(a), iodine release in NaCl  
255 solution gradually increased over time, reaching a maximum rate near 0.8 mmol/m<sup>2</sup>/d at  
256 day 11, and then slightly decreased near the end of the 14-day test. The Pb and V release  
257 exhibited similar patterns with a relatively high initial rate around 0.075 mmol/m<sup>2</sup>/d, then  
258 gradually decreased, and eventually approached a plateau near 0.05 mmol/m<sup>2</sup>/d. In Fig.  
259 6(b), the release patterns of iodine and vanadium in Na<sub>2</sub>CO<sub>3</sub> are similar: release rates  
260 rapidly reached maximum near day 2 and then gradually decreased over time approaching  
261 a plateau. However, the long-term rate of Pb in Na<sub>2</sub>CO<sub>3</sub> appears to be constant. In Fig.  
262 6(c), the iodine release in Na<sub>2</sub>SO<sub>4</sub> exhibited a high initial rate approximately 0.32  
263 mmol/m<sup>2</sup>/d and then its rate gradually decreased, eventually approaching a plateau around  
264 0.15 mmol/m<sup>2</sup>/d. Despite no high initial release, the Pb and V release patterns follow the

265 trend of iodine release: gradually decreased over time and then rebounded near day 10.  
266 The Fig. 6(d) describes the element release of iodoapatite in  $\text{Na}_3\text{PO}_4$ , which shows  
267 constant rates of  $\sim 4.5$ ,  $\sim 3.5$ , and  $\sim 13$   $\text{mmol}/\text{m}^2/\text{d}$  for the release for iodine, Pb, and V,  
268 respectively. Due to the instrumentation limitation and sample consumption, only four  
269 leachates from the  $\text{Na}_3\text{PO}_4$  experiment was analyzed for their Pb content.

270 Leaching rates of I, Pb, and V based on the solutions analysis are compared in Figs.  
271 7(a-c), respectively. In general, leaching tests conducted in the ionic solutions present  
272 significantly higher element release rates than those of deionized water in the order of  
273  $\text{Na}_3\text{PO}_4 > \text{Na}_2\text{CO}_3 > \text{Na}_2\text{SO}_4 > \text{water}$ , except in the NaCl solution. In Fig. 7(a), iodine  
274 release from  $\text{Na}_3\text{PO}_4$ ,  $\text{Na}_2\text{CO}_3$ , and  $\text{Na}_2\text{SO}_4$  solutions exhibited a long-term leach pattern  
275 similar to that of water leaching: started with a high initial release, then gradually  
276 decreased, and eventually stabilized and reached a plateau. The iodine release in NaCl  
277 solution, however, presents a different pattern: iodine rate increased from the beginning  
278 of leach test to day 11, when the rate reached maximum and then stabilized. The release  
279 rates of Pb and V from NaCl test are relatively constant but not higher than those of water  
280 leached as shown in Figs. 7(b, c).

281 The molar ratios in leachate solutions are illustrated in Figs. 7(d, e). Except for the  
282 anomalous NaCl data, the long-term I/V ratios in Fig. 7(d) fluctuate around the ratio of  
283 water-leached sample within the range of  $[0.34, 1.02]$ , which are higher than the  
284 stoichiometric value 0.28. In Fig. 7(e), the long-term Pb/V ratios of NaCl and  $\text{Na}_2\text{SO}_4$   
285 tests are 1.36 and 1.65, approximate to the stoichiometric value 1.64, whereas the long-  
286 term ratios from  $\text{Na}_2\text{CO}_3$  and  $\text{Na}_3\text{PO}_4$  tests are 0.95 and 0.27, significantly lower than  
287 1.64.

### 288        **3.5 Overview of leaching rates in solutions**

289        The phases of interest in this study are the aqueous solutions and the solid surfaces.  
290        The leachate solution chemistry in Fig. 7 shows that iodine release from the sample  
291        leached by the NaCl solution has a distinctive pattern. For the other leach tests, the long-  
292        term iodine rates (plateau region in Figs. 6-7) are at least one magnitude higher than that  
293        from water leaching. And the order of iodine leach rate, based on solution analysis in Fig  
294        7 (a), is consistent with the orders of Pb and V rates in Fig. 7 (b, c):  $R_{\text{Pb/V/I}}(\text{Na}_3\text{PO}_4) >$   
295         $R_{\text{Pb/V/I}}(\text{Na}_2\text{CO}_3) > R_{\text{Pb/V/I}}(\text{Na}_2\text{SO}_4) > R_{\text{Pb/V/I}}(\text{deionized water})$ . In the following section,  
296        we will analyze the anomalous result of NaCl leach test and then explain how element  
297        release behaviors differentiate due to the different solution chemistry, such as pH and  
298        ionic species.

## 299        **4 Discussion**

### 300        **4.1 Anomaly of the sample leached by NaCl solution**

301        Iodoapatite sample leached by 0.1 mol/L NaCl solution exhibited unique surface  
302        phase composition and iodine release pattern. The XRD data in Figs. 4 and 5 show  
303        leached surface has no apparent splitting in the region from  $25^\circ$  to  $28^\circ$  ( $2\theta$ ) and a new  
304        peak ( $\bar{1}\bar{3}1$ ), attributed by a vanadinite phase. This anomaly suggests a reduced structural  
305        distortion, which can be contributed by substituting iodide with smaller chloride. The  
306        refinement in Fig. 5 confirmed new phase vanadinite was formed on the surface, which  
307        resembles the XRD pattern of iodoapatite  $\text{Pb}_{9.85}(\text{VO}_4)_6\text{I}_{1.7}$ . The XRD data is consistent  
308        with the EDS result and solution analysis. The Pb EDS band at 2.6 keV, in Fig 2, is  
309        comparatively enhanced due to the overlap by chlorine signal at 2.6 keV. The release



310 rates of iodine from the NaCl test in Fig. 6(a) suggest the new phase was growing until  
311 the equilibrium state was reached. A similar iodine release pattern was observed in a pH 4  
312 semi-dynamic leaching experiment, of which the rate anomaly was caused by the  
313 formation of a secondary phase.<sup>37</sup> The molar ratios of Pb/V in Fig. 7(e) approximate to  
314 the stoichiometric value 1.6, indicating a congruent dissolution of Pb and V. The variation  
315 of I/V molar ratios in Fig. 7(d) is consistent with that of iodine rates in Fig. 6(a). Both the  
316 I/V ratios and iodine rates suggest an incongruent release for iodine, unlike the congruent  
317 Pb and V. The SEM images in Figs. 1(b, e) show that both surfaces leached by NaCl and  
318 deionized water share similar morphology. The new phase vanadinite  $Pb_5(VO_4)_3Cl$ ,  
319 confirmed by the XRD refinement, suggests ion-exchange process between iodide and  
320 chloride. This postulation is supported by the solution and surface analysis that 1) a  
321 significant amount of iodine was released into NaCl solution while the Pb and V rates are  
322 comparable to the data of water leach test as shown in Figs. 6-7; 2) the surface alteration  
323 revealed by SEM in Fig. 1 and the surface chemistry by EDS in Fig. 2 resemble those of  
324 deionized water. Interestingly, the structural deformation of the original iodine-bearing  
325 apatite  $Pb_{9.85}(VO_4)_6I_{1.7}$  appeared to be restored in the chlorine-substituted structure  
326 vanadinite  $Pb_5(VO_4)_3Cl$ . Given that the ionic radius of chloride ( $Cl^-$ ,  $1.68 \pm 0.19 \text{ \AA}$ ) is  
327 considerably smaller than that of iodide ( $I^-$ ,  $2.11 \pm 0.19 \text{ \AA}$ ),<sup>46</sup> exchanging the iodide with  
328 smaller chloride seems to have repaired the structural deformation.

#### 329 **4.2 Effect of pH on iodine release and secondary phase formation**

330 The solution pH has a strong effect on the iodine release of the iodoapatite. Chemical  
331 properties of the leaching solutions calculated by VMINTEQ are listed in Table 2.  
332 According to our previous studies, iodoapatite dissolution in deionized water can be

333 represented by the congruent release of Pb and V.<sup>29</sup> In Fig. 7 (b, c), the Pb and V rates  
334 from different solutions are generally constant, indicating a constant-dissolution  
335 controlled process. The overall dissolution rates from low to high appears to be:  $R$   
336 (*deionized water*) <  $R$  ( $Na_2SO_4$ ) <  $R$  ( $Na_2CO_3$ ) <  $R$  ( $Na_3PO_4$ ), which corresponds to the  
337 solution pH values ~6.1, ~6.2, ~10.3, and ~10.9 under 90 °C as listed in Table 2.  
338 Therefore, increasing pH from neutral to basic can increase the iodine release by  
339 enhancing the overall dissolution of the iodoapatite, which is consistent with previous  
340 experimental results on synthetic iodoapatite and natural apatites<sup>33,47</sup>. However, due to the  
341 secondary phase formed in  $Na_2CO_3$  solutions, the dissolution process was being  
342 continuously hindered by the accumulating precipitates. Interestingly, the trend of iodine  
343 released in  $Na_2CO_3$  solution of pH 10.3 resembles that of leaching iodoapatite under pH  
344 4.<sup>37</sup> Despite the rate difference, both surfaces leached by pH 4 and pH 10.3 formed  
345 secondary phases (chervetite and hydroxylvanadinite, respectively). Our previous study  
346 showed that the equivalent long-term rate of iodine release under pH 6 is 8.1 mmol/m<sup>2</sup>/d,  
347 over two magnitudes higher than that of the deionized water 0.036 mmol/m<sup>2</sup>/d.<sup>37</sup>  
348 Nevertheless, the release rates of iodine leached by the solutions of non-neutral pH are at  
349 least one magnitude higher than that of the neutral pH solutions due to the enhanced  
350 dissolution process.

351 Surface characterizations indicate the presence of new phases under the basic  
352 conditions. The XRD analysis in Fig. 4 and Table 1 shows the surfaces leached by the  
353  $Na_2CO_3$  and  $Na_3PO_4$  solutions were dominated by secondary phases resembling  
354 hydroxylvanadinite  $Pb_{10}(VO_4)_6(OH)_2$ . The SEM in Fig. 1 reveals different grain shapes  
355 and sizes from the water leached, while the EDS in Fig. 2 demonstrates that iodine was

356 depleted on the surface. The solution analysis also supports the formation of new phase  
357 given the similar element release pattern to that of pH 4 and incongruent Pb/V ratios far  
358 away from the stoichiometric value. As shown in Fig. 7, the leaching rates of all elements  
359 are at least one magnitude higher than the water leach rates of corresponding elements.  
360 The results from this study and those from relevant literature suggest that the solution pH  
361 exerts significant effects on the dissolution rate and the secondary phase formation in  
362 aqueous environments such as chervetite and hydroxyvanadinite precipitated under acidic  
363 and basic conditions, respectively.<sup>37,48,49</sup>

#### 364 **4.3 Effect of ionic species on the dissolution rate**

365 In this study, dissolved species affected the sample dissolution process by increasing  
366 the ionic strength in solution, which consequently reduced the activity coefficient of  
367 dissolved species. As a result, saturation state and solution feedback were reduced, which  
368 in return increased the dissolution rate.<sup>47</sup> Although the 0.1 mol/L Na<sub>2</sub>SO<sub>4</sub> and 0.1 mol/L  
369 NaCl solutions have approximately the same solution pH as deionized water, the  
370 dissolution rates in these ionic solutions are significantly higher than that of the deionized  
371 water. As shown in Table 2, 0.1 mol/L Na<sub>2</sub>SO<sub>4</sub> solution gives total ionic strength of 0.26  
372 mol/L, 0.1 mol/L NaCl solution 0.098 mol/L, and deionized water  $2.04 \times 10^{-6}$  mol/L close  
373 to zero. The vast difference in ionic strength leads to different degrees of saturation state.  
374 The activity coefficient of the major ions Na<sup>+</sup>, Cl<sup>-</sup>, and SO<sub>4</sub><sup>2-</sup> in these ionic solutions are  
375 ranging from 0.25 to 0.76, considerably lower than the major ions H<sup>+</sup> and OH<sup>-</sup> with a  
376 respective activity coefficient 1.00 in the deionized water. The dissolution rate in 0.1  
377 mol/L Na<sub>2</sub>SO<sub>4</sub> solution is higher than the rate in the 0.1 mol/L NaCl solution and  
378 deionized water under the same pH and reaction mechanism, as shown in Fig. 7.

379 Moreover, the average release rate of iodine in Na<sub>3</sub>PO<sub>4</sub> (pH 10.9) is about one magnitude  
380 higher than that of Na<sub>2</sub>CO<sub>3</sub> (pH 10.3) despite their similar pHs. The difference in rates can be  
381 inferred from the difference in ionic strength: 0.29 mol/L for 0.1 mol/L Na<sub>3</sub>PO<sub>4</sub> and 0.25  
382 mol/L for Na<sub>2</sub>CO<sub>3</sub> solution.

383 In addition, no substantial structure change happened to the sample leached by 0.1  
384 mol/L Na<sub>2</sub>SO<sub>4</sub> solution. It is unlikely that anion SO<sub>4</sub><sup>2-</sup> can be incorporated into apatite  
385 structure as there is no evidence from surface characterization and solution analysis to  
386 support that. No structural change was detected by the XRD characterization. The SEM  
387 images and EDS analysis in Figs. 1 and 2 show that the Na<sub>2</sub>SO<sub>4</sub> and water leached  
388 surfaces have a similar grain size, surface morphology, and chemical composition. The  
389 element release rates and ratios in Fig. 7 and 8 demonstrate a similar leach behavior  
390 between samples leached by Na<sub>2</sub>SO<sub>4</sub> and deionized water. The similarities in surface  
391 alteration and leaching behavior between samples leached by Na<sub>2</sub>SO<sub>4</sub> and water suggest  
392 that the iodine release in Na<sub>2</sub>SO<sub>4</sub> solution was controlled by short-term diffusion and  
393 long-term dissolution and the release of Pb and V is controlled by congruent dissolution.  
394 No precipitated was observed on Na<sub>2</sub>SO<sub>4</sub> leached surface, which is also similar to the  
395 surface leached by water.

396 In terms of the surface precipitation, the SEM images in Figs. 1 (c, f) reflect intense  
397 surface alterations in the solutions of Na<sub>3</sub>PO<sub>4</sub> and Na<sub>2</sub>CO<sub>3</sub>. The leached surfaces yielded  
398 XRD patterns similar to the standard hydroxyvanadinite Pb<sub>5</sub>(VO<sub>4</sub>)<sub>3</sub>OH. However,  
399 significant contractions of *a*- and *b*-axes as shown in Table 2 indicate the size of VO<sub>4</sub> site  
400 was reduced, which could be caused by a substitution of smaller groups.<sup>50</sup> The IR  
401 spectroscopy of the sample leached by Na<sub>3</sub>PO<sub>4</sub> confirms the existence of P-O bond and

402 OH<sup>-</sup>. Furthermore, the EDS detected phosphorus signal, which also supports that PO<sub>4</sub>  
403 group was in VO<sub>4</sub> site. The molar ratios of Pb/V in Fig. 7 show a deficiency of Pb relative  
404 to V in Na<sub>3</sub>PO<sub>4</sub> leaching test. These evidences suggest the precipitates are a product of  
405 hydroxyvanadinite with mixed site: Pb<sub>10</sub>(VO<sub>4</sub>)<sub>n</sub>(PO<sub>4</sub>)<sub>6-n</sub>(OH)<sub>2</sub>. The site mixing is possible  
406 since Pb<sub>10</sub>(VO<sub>4</sub>)<sub>x</sub>(PO<sub>4</sub>)<sub>6-x</sub>(OH)<sub>2</sub> can occur during wet chemistry reactions under similar  
407 conditions.<sup>48</sup> Carbonate is known to be incorporated into apatite structure by  
408 substitution.<sup>50-53</sup> Given that phosphate (PO<sub>4</sub><sup>3-</sup>, ionic radius 2.30 ± 0.42 Å)<sup>46</sup> can replace  
409 vanadate in iodoapatite,<sup>48</sup> it is reasonable to presume that carbonate of a smaller ionic  
410 radius (CO<sub>3</sub><sup>2-</sup>, 1.89 ± 0.19 Å)<sup>46</sup> can substitute vanadate in a similar crystal structure.  
411 Therefore, the secondary phase formed on in the Na<sub>2</sub>CO<sub>3</sub> solution is Pb<sub>10</sub>(VO<sub>4</sub>)<sub>6-</sub>  
412 <sub>m</sub>(CO<sub>3</sub>)<sub>1.5m</sub>(OH)<sub>2</sub>.

#### 413 **4.4 Mechanism of iodoapatite dissolution and surface reactions in aqueous** 414 **environments**

415 Fig. 8 generalizes the mechanism of iodoapatite dissolutions with multiple processes  
416 contributing to the iodine release. Our previous study on iodine release in deionized water  
417 suggests that the iodine release is driven by short-term diffusion and long-term  
418 dissolution.<sup>29</sup> Diffusion and dissolution are affected by various factors of the solution  
419 chemistry, such as solution ionic strength, pH, and secondary phase formation resulted  
420 from a supersaturation of the solution with respect to low solubility species. In neutral pH  
421 solutions, the iodine release is subjected to the substitution of iodine by anionic species in  
422 solution such as OH<sup>-</sup> and Cl<sup>-</sup>. When dealing with solutions of comparable pH, a higher  
423 ionic strength, due to the ionic content, can enhance the dissolution by changing  
424 saturation conditions. Solution pH other than near neutral can increase the dissolution by

425 exponentially accelerating the dissolution process. The resulting rapid dissolution can  
426 often lead to the precipitation of secondary phases when the solution approaches the  
427 supersaturation state of low solubility phases. Possible secondary phases include  
428 chervetite  $\text{Pb}_2\text{V}_2\text{O}_7$  under acidic condition<sup>37</sup> and hydroxylvanadinite  $\text{Pb}_5(\text{VO}_4)_3\text{OH}$  under  
429 basic condition.

## 430 **5 Conclusions**

431 The present study focuses on effects by solution compositions on iodoapatite  
432 dissolution. The results suggest that the higher ionic strength can accelerate dissolution by  
433 decreasing the activity coefficient of reacting aqueous species, thus promoting iodine  
434 release from apatite. Non-neutral pH conditions clearly increase the dissolution rate and  
435 often lead to precipitations of secondary phases, such as chervetite and  
436 hydroxylvanadinite. The secondary phase precipitation at the surfaces hinders the  
437 dissolution rate by reducing the available reacting surface area. However, the overall  
438 iodine release rates in both basic and acidic solutions are exponentially higher than those  
439 in the near-neutral pH conditions, especially in deionized water. Current understanding of  
440 dissolution is mostly based on leaching experiments conducted in deionized water. Our  
441 investigation on the impact of solution chemistry reveals new complexities of the  
442 dissolution kinetics of crystalline waste form during environmental degradation, Unlike  
443 fresh water with low ion content, high concentrations of aqueous species commonly  
444 found in underground brines can compromise the chemical durability of crystalline waste  
445 form in a geological repository. For this specific waste form, maintaining neutral pH and  
446 low ion content in aqueous solutions is important to the disposal safety of radioactive  
447 iodine. Since iodine is one of the most challenging radionuclides to immobilize, building

448 a comprehensive theoretical framework of iodine immobilization can significantly  
449 advance the research in nuclear waste disposal safety.

### 450 **Conflicts of interest**

451 There are no conflicts to declare.

### 452 **Acknowledgements**

453 This work was supported as part of the Center for Performance and Design of Nuclear  
454 Waste Forms and Containers, an Energy Frontier Research Center funded by the U.S.  
455 Department of Energy, Office of Science, Basic Energy Sciences (DE-SC0016584). The  
456 sample surface characterizations were carried out at the Shared Instrumentation Facilities  
457 (SIF) and Center for Advanced Microstructures and Devices (CAMD) of Louisiana State  
458 University. We thank our XRD & Geochemistry Lab Researcher Wanda LeBlanc for  
459 operating XRD experiments at SIF and facilitating our experiments in Geochemistry Lab.  
460 We also thank Dr. Orhan Kizilkaya from CAMD for his assistance on infrared  
461 spectroscopy.

### 462 **Date Availability**

463 Data will be made available on request

464 **References**

- 465 (1) Climate Change 2014: Mitigation of Climate Change: Working Group III Contribution to the Fifth  
466 Assessment Report of the Intergovernmental Panel on Climate Change; Intergovernmental Panel  
467 on Climate Change, Edenhofer, O., Eds.; Cambridge University Press: New York, NY, 2014.
- 468 (2) Alley, W. M.; Alley, R. The Growing Problem of Stranded Used Nuclear Fuel. *Environ. Sci. Technol.*  
469 **2014**, 48 (4), 2091–2096. <https://doi.org/10.1021/es405114h>.
- 470 (3) Nichols, A. L.; Verpelli, M.; Aldama, D. L. Handbook of Nuclear Data for Safeguards; INDC(NDS)--  
471 0502; International Atomic Energy Agency, 2007.
- 472 (4) Ojovan, M. I.; Lee, W. E. 10 - Long-Lived Waste Radionuclides. In *An Introduction to Nuclear  
473 Waste Immobilisation (Second Edition)*; Ojovan, M. I., Lee, W. E., Eds.; Elsevier: Oxford, 2014; pp  
474 107–115. <https://doi.org/10.1016/B978-0-08-099392-8.00010-3>.
- 475 (5) Aimoz, L.; Wieland, E.; Taviot-Guého, C.; Dähn, R.; Vespa, M.; Churakov, S. V. Structural Insight  
476 into Iodide Uptake by AFm Phases. *Environ. Sci. Technol.* **2012**, 46 (7), 3874–3881.  
477 <https://doi.org/10.1021/es204470e>.
- 478 (6) Um, W.; Serne, R. J.; Krupka, K. M. Linearity and Reversibility of Iodide Adsorption on Sediments  
479 from Hanford, Washington under Water Saturated Conditions. *Water Res.* **2004**, 38 (8), 2009–  
480 2016. <https://doi.org/10.1016/j.watres.2004.01.026>.
- 481 (7) Coughtrey, P. J.; Thorne, M. C. Radionuclide Distribution and Transport in Terrestrial and Aquatic  
482 Ecosystems. A Critical Review of Data; 1983; Vol. 1.
- 483 (8) Whitehead, D. C. The Distribution and Transformations of Iodine in the Environment. *Environ. Int.*  
484 **1984**, 10 (4), 321–339. [https://doi.org/10.1016/0160-4120\(84\)90139-9](https://doi.org/10.1016/0160-4120(84)90139-9).
- 485 (9) Schwehr, K. A.; Santschi, P. H.; Kaplan, D. I.; Yeager, C. M.; Brinkmeyer, R. Organo-Iodine  
486 Formation in Soils and Aquifer Sediments at Ambient Concentrations. *Environ. Sci. Technol.* **2009**,  
487 43 (19), 7258–7264. <https://doi.org/10.1021/es900795k>.
- 488 (10) Shimamoto, Y. S.; Takahashi, Y.; Terada, Y. Formation of Organic Iodine Supplied as Iodide in a  
489 Soil–Water System in Chiba, Japan. *Environ. Sci. Technol.* **2011**, 45 (6), 2086–2092.  
490 <https://doi.org/10.1021/es1032162>.
- 491 (11) Fuge, R.; Johnson, C. C. Iodine and Human Health, the Role of Environmental Geochemistry and  
492 Diet, a Review. *Appl. Geochem.* **2015**, 63, 282–302.  
493 <https://doi.org/10.1016/j.apgeochem.2015.09.013>.
- 494 (12) Patrick, L. Iodine: Deficiency and Therapeutic Considerations. *Altern. Med. Rev.* **2008**, 13 (2), 116–  
495 127.
- 496 (13) Audubert, F.; Carpena, J.; Lacout, J. L.; Tetard, F. Elaboration of an Iodine-Bearing Apatite Iodine  
497 Diffusion into a Pb<sub>3</sub>(VO<sub>4</sub>)<sub>2</sub> Matrix. *Solid State Ion.* **1997**, 95 (1), 113–119.  
498 [https://doi.org/10.1016/S0167-2738\(96\)00570-X](https://doi.org/10.1016/S0167-2738(96)00570-X).
- 499 (14) Garino, T. J.; Nenoff, T. M.; Krumhansl, J. L.; Rademacher, D. X. Low-Temperature Sintering Bi–Si–  
500 Zn-Oxide Glasses for Use in Either Glass Composite Materials or Core/Shell 129I Waste Forms. *J.*  
501 *Am. Ceram. Soc.* **2011**, 94 (8), 2412–2419. <https://doi.org/10.1111/j.1551-2916.2011.04542.x>.
- 502 (15) Krumhansl, J. L.; Nenoff, T. M. Hydrotalcite-like Layered Bismuth–Iodine–Oxides as Waste Forms.  
503 *Applied Geochemistry* **2011**, 26 (1), 57–64. <https://doi.org/10.1016/j.apgeochem.2010.11.003>.
- 504 (16) Sava, D. F.; Garino, T. J.; Nenoff, T. M. Iodine Confinement into Metal–Organic Frameworks  
505 (MOFs): Low-Temperature Sintering Glasses To Form Novel Glass Composite Material (GCM)  
506 Alternative Waste Forms. *Ind. Eng. Chem. Res.* **2012**, 51 (2), 614–620.  
507 <https://doi.org/10.1021/ie200248g>.
- 508 (17) Sava, D. F.; Rodriguez, M. A.; Chapman, K. W.; Chupas, P. J.; Greathouse, J. A.; Crozier, P. S.;  
509 Nenoff, T. M. Capture of Volatile Iodine, a Gaseous Fission Product, by Zeolitic Imidazolate



510 Framework-8. *J. Am. Chem. Soc.* **2011**, 133 (32), 12398–12401.  
511 <https://doi.org/10.1021/ja204757x>.

512 (18) Riley, B. J.; Vienna, J. D.; Strachan, D. M.; McCloy, J. S.; Jerden, J. L. Materials and Processes for  
513 the Effective Capture and Immobilization of Radioiodine: A Review. *J. Nucl. Mater.* **2016**, 470,  
514 307–326. <https://doi.org/10.1016/j.jnucmat.2015.11.038>.

515 (19) Frankel, G. S.; Vienna, J. D.; Lian, J.; Scully, J. R.; Gin, S.; Ryan, J. V.; Wang, J.; Kim, S. H.; Windl, W.;  
516 Du, J. A Comparative Review of the Aqueous Corrosion of Glasses, Crystalline Ceramics, and  
517 Metals. *npj Materials Degradation* **2018**, 2 (1), 15. <https://doi.org/10.1038/s41529-018-0037-2>.

518 (20) Faucon, P.; Adenot, F.; Jacquinet, J. F.; Petit, J. C.; Cabrillac, R.; Jorda, M. Long-Term Behaviour of  
519 Cement Pastes Used for Nuclear Waste Disposal: Review of Physico-Chemical Mechanisms of  
520 Water Degradation. *Cem. Concr. Res.* **1998**, 28 (6), 847–857. [https://doi.org/10.1016/S0008-](https://doi.org/10.1016/S0008-8846(98)00053-2)  
521 [8846\(98\)00053-2](https://doi.org/10.1016/S0008-8846(98)00053-2).

522 (21) Frankel, G. S.; Vienna, J.; Lian, J. WastePD, an Innovative Center on Materials Degradation. *npj*  
523 *Mater. Degrad.* **2017**, 1 (1), 5. <https://doi.org/10.1038/s41529-017-0002-5>.

524 (22) Chapman, N. A.; McKinley, I. G.; Smellie, J. a. T. The Potential of Natural Analogues in Assessing  
525 Systems for Deep Disposal of High-Level Radioactive Waste; EIR--545; Eidgenossisches Inst. fuer  
526 Reaktorforschung: Sweden, 1984.

527 (23) Kato, H.; Kato, O.; Tanabe, H. Review of Immobilization Techniques of Radioactive Iodine for  
528 Geological Disposal. **2002**. <https://doi.org/10.11484/JAERI-Conf-2002-004>.

529 (24) Chapman, K. W.; Chupas, P. J.; Nenoff, T. M. Radioactive Iodine Capture in Silver-Containing  
530 Mordenites through Nanoscale Silver Iodide Formation. *J. Am. Chem. Soc.* **2010**, 132 (26), 8897–  
531 8899. <https://doi.org/10.1021/ja103110y>.

532 (25) Yao, T.; Lu, F.; Sun, H.; Wang, J.; Ewing, R. C.; Lian, J. Bulk Iodoapatite Ceramic Densified by Spark  
533 Plasma Sintering with Exceptional Thermal Stability. *J. Am. Ceram. Soc.* **2014**, 97 (8), 2409–2412.  
534 <https://doi.org/10.1111/jace.13101>.

535 (26) Maddrell, E.; Gandy, A.; Stennett, M. The Durability of Iodide Sodalite. *Journal of Nuclear*  
536 *Materials* **2014**, 449 (1), 168–172. <https://doi.org/10.1016/j.jnucmat.2014.03.016>.

537 (27) Chong, S.; Peterson, J. A.; Riley, B. J.; Tabada, D.; Wall, D.; Corkhill, C. L.; McCloy, J. S. Glass-  
538 Bonded Iodosodalite Waste Form for Immobilization of <sup>129</sup>I. *J. Nucl. Mater.* **2018**, 504, 109–121.  
539 <https://doi.org/10.1016/j.jnucmat.2018.03.033>.

540 (28) Le Gallet, S.; Campayo, L.; Courtois, E.; Hoffmann, S.; Grin, Yu.; Bernard, F.; Bart, F. Spark Plasma  
541 Sintering of Iodine-Bearing Apatite. *J. Nucl. Mater.* **2010**, 400 (3), 251–256.  
542 <https://doi.org/10.1016/j.jnucmat.2010.03.011>.

543 (29) Zhang, Z.; Heath, A.; T. Valsaraj, K.; L. Ebert, W.; Yao, T.; Lian, J.; Wang, J. Mechanism of Iodine  
544 Release from Iodoapatite in Aqueous Solution. *RSC Adv.* **2018**, 8 (8), 3951–3957.  
545 <https://doi.org/10.1039/C7RA11049A>.

546 (30) Gauthier-Lafaye, F. 2 Billion Year Old Natural Analogs for Nuclear Waste Disposal: The Natural  
547 Nuclear Fission Reactors in Gabon (Africa). *C. R. Phys.* **2002**, 3 (7), 839–849.  
548 [https://doi.org/10.1016/S1631-0705\(02\)01351-8](https://doi.org/10.1016/S1631-0705(02)01351-8).

549 (31) Uno, M.; Shinohara, M.; Kurosaki, K.; Yamanaka, S. Some Properties of a Lead Vanado-  
550 Iodoapatite Pb<sub>10</sub>(VO<sub>4</sub>)<sub>6</sub>I<sub>2</sub>. *J. Nucl. Mater.* **2001**, 294 (1), 119–122.  
551 [https://doi.org/10.1016/S0022-3115\(01\)00462-7](https://doi.org/10.1016/S0022-3115(01)00462-7).

552 (32) National Research Council. Scho; 2011. <https://doi.org/10.17226/13100>.

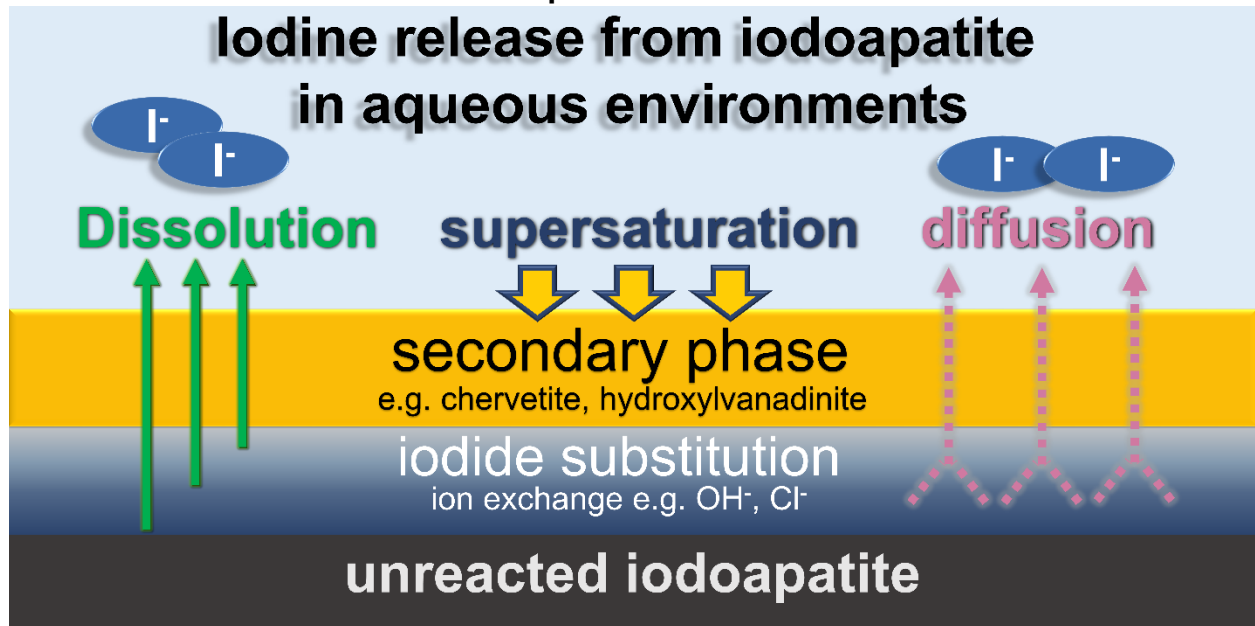
553 (33) Guy, C.; Audubert, F.; Lartigue, J.-E.; Latriille, C.; Advocat, T.; Fillet, C. New Conditionings for  
554 Separated Long-Lived Radionuclides. *C. R. Phys.* **2002**, 3 (7), 827–837.  
555 [https://doi.org/10.1016/S1631-0705\(02\)01377-4](https://doi.org/10.1016/S1631-0705(02)01377-4).

- 556 (34) Zhang, M.; Maddrell, E. R.; Abruaitis, P. K.; Salje, E. K. H. Impact of Leach on Lead Vanado-  
557 Iodoapatite [Pb<sub>5</sub>(VO<sub>4</sub>)<sub>3</sub>I]: An Infrared and Raman Spectroscopic Study. *Mater. Sci. Eng. B* **2007**,  
558 137 (1), 149–155. <https://doi.org/10.1016/j.mseb.2006.11.003>.
- 559 (35) Coulon, A.; Grandjean, A.; Laurencin, D.; Jollivet, P.; Rossignol, S.; Campayo, L. Durability Testing  
560 of an Iodate-Substituted Hydroxyapatite Designed for the Conditioning of 129I. *J. Nucl. Mater.*  
561 **2017**, 484, 324–331. <https://doi.org/10.1016/j.jnucmat.2016.10.047>.
- 562 (36) ASTM C1220-17, Standard Test Method for Static Leaching of Monolithic Waste Forms for  
563 Disposal of Radioactive Waste; ASTM International: West Conshohocken, PA, 2017.
- 564 (37) Zhang, Z.; Ebert, W. L.; Yao, T.; Lian, J.; Valsaraj, K. T.; Wang, J. Chemical Durability and  
565 Dissolution Kinetics of Iodoapatite in Aqueous Solutions. *ACS Earth Space Chem.* **2019**, 3 (3), 452-  
566 462. <https://doi.org/10.1021/acsearthspacechem.8b00162>.
- 567 (38) Zhu, Y.; Zhang, X.; Chen, Y.; Xie, Q.; Lan, J.; Qian, M.; He, N. A Comparative Study on the  
568 Dissolution and Solubility of Hydroxylapatite and Fluorapatite at 25°C and 45°C. *Chem. Geol.*  
569 **2009**, 268 (1), 89–96. <https://doi.org/10.1016/j.chemgeo.2009.07.014>.
- 570 (39) Cazalbou, S.; Eichert, D.; Ranz, X.; Drouet, C.; Combes, C.; Harmand, M. F.; Rey, C. Ion Exchanges  
571 in Apatites for Biomedical Application. *J. Mater. Sci. Mater. Med.* **2005**, 16 (5), 405–409.  
572 <https://doi.org/10.1007/s10856-005-6979-2>.
- 573 (40) Brenan, J. Kinetics of Fluorine, Chlorine and Hydroxyl Exchange in Fluorapatite. *Chem. Geol.* **1993**,  
574 110 (1), 195–210. [https://doi.org/10.1016/0009-2541\(93\)90254-G](https://doi.org/10.1016/0009-2541(93)90254-G).
- 575 (41) Dorozhkin, S. V. A Review on the Dissolution Models of Calcium Apatites. *Prog. Cryst. Growth*  
576 *Charact.* **2002**, 44 (1), 45–61. [https://doi.org/10.1016/S0960-8974\(02\)00004-9](https://doi.org/10.1016/S0960-8974(02)00004-9).
- 577 (42) Petříček, V.; Dušek, M.; Palatinus, L. Crystallographic Computing System JANA2006: General  
578 Features. *Z. Kristallogr. Cryst. Mater.* **2014**, 229 (5), 345–352. <https://doi.org/10.1515/zkri-2014-1737>.
- 580 (43) Audubert, F.; Savariault, J.-M.; Lacout, J.-L. Pentalead Tris(Vanadate) Iodide, a Defect Vanadinite-  
581 Type Compound. *Acta Crystallogr. C* **1999**, 55 (3), 271–273.  
582 <https://doi.org/10.1107/S0108270198005034>.
- 583 (44) Ślósarczyk, A.; Paszkiewicz, Z.; Paluszkiwicz, C. FTIR and XRD Evaluation of Carbonated  
584 Hydroxyapatite Powders Synthesized by Wet Methods. *J. Mol. Struct.* **2005**, 744–747, 657–661.  
585 <https://doi.org/10.1016/j.molstruc.2004.11.078>.
- 586 (45) Merry, J. C.; Gibson, I. R.; Best, S. M.; Bonfield, W. Synthesis and Characterization of Carbonate  
587 Hydroxyapatite. *J. Mater. Sci. Mater. Med.* **1998**, 9 (12), 779–783.  
588 <https://doi.org/10.1023/A:1008975507498>.
- 589 (46) Roobottom, H. K.; Jenkins, H. D. B.; Passmore, J.; Glasser, L. Thermochemical Radii of Complex  
590 Ions. *J. Chem. Educ.* **1999**, 76 (11), 1570. <https://doi.org/10.1021/ed076p1570>.
- 591 (47) Guidry, M. W.; Mackenzie, F. T. Experimental Study of Igneous and Sedimentary Apatite  
592 Dissolution: Control of PH, Distance from Equilibrium, and Temperature on Dissolution Rates.  
593 *Geochim. Cosmochim. Acta* **2003**, 67 (16), 2949–2963. [https://doi.org/10.1016/S0016-7037\(03\)00265-5](https://doi.org/10.1016/S0016-7037(03)00265-5).
- 595 (48) Cao, C.; Chong, S.; Thirion, L.; C. Mauro, J.; S. McCloy, J.; Goel, A. Wet Chemical Synthesis of  
596 Apatite-Based Waste Forms – A Novel Room Temperature Method for the Immobilization of  
597 Radioactive Iodine. *J. Mater. Chem. C* **2017**, 5 (27), 14331–14342.  
598 <https://doi.org/10.1039/C7TA00230K>.
- 599 (49) Campayo, L.; Audubert, F.; Lartigue, J.-E.; Courtois-Manara, E.; Gallet, S. L.; Bernard, F.; Lemesle,  
600 T.; Mear, F. O.; Montagne, L.; Coulon, A.; et al. French Studies on the Development of Potential  
601 Conditioning Matrices for Iodine 129. *Mater. Res. Soc. Symp. Proc.* **2015**, 1744, 15–20.  
602 <https://doi.org/10.1557/opl.2015.309>.

- 603 (50) Zapanta-Legeros, R. Effect of Carbonate on the Lattice Parameters of Apatite. *Nature* **1965**, 206  
604 (4982), 403. <https://doi.org/10.1038/206403a0>.
- 605 (51) White, T. J.; Dong, Z. L. Structural Derivation and Crystal Chemistry of Apatites. *Acta Cryst. B*  
606 **2003**, 59 (1), 1–16. <https://doi.org/10.1107/S0108768102019894>.
- 607 (52) Fleet, M. E.; Liu, X. Coupled Substitution of Type A and B Carbonate in Sodium-Bearing Apatite.  
608 *Biomaterials* **2007**, 28 (6), 916–926. <https://doi.org/10.1016/j.biomaterials.2006.11.003>.
- 609 (53) Landi, E.; Tampieri, A.; Celotti, G.; Vichi, L.; Sandri, M. Influence of Synthesis and Sintering  
610 Parameters on the Characteristics of Carbonate Apatite. *Biomaterials* **2004**, 25 (10), 1763–1770.  
611 <https://doi.org/10.1016/j.biomaterials.2003.08.026>.  
612

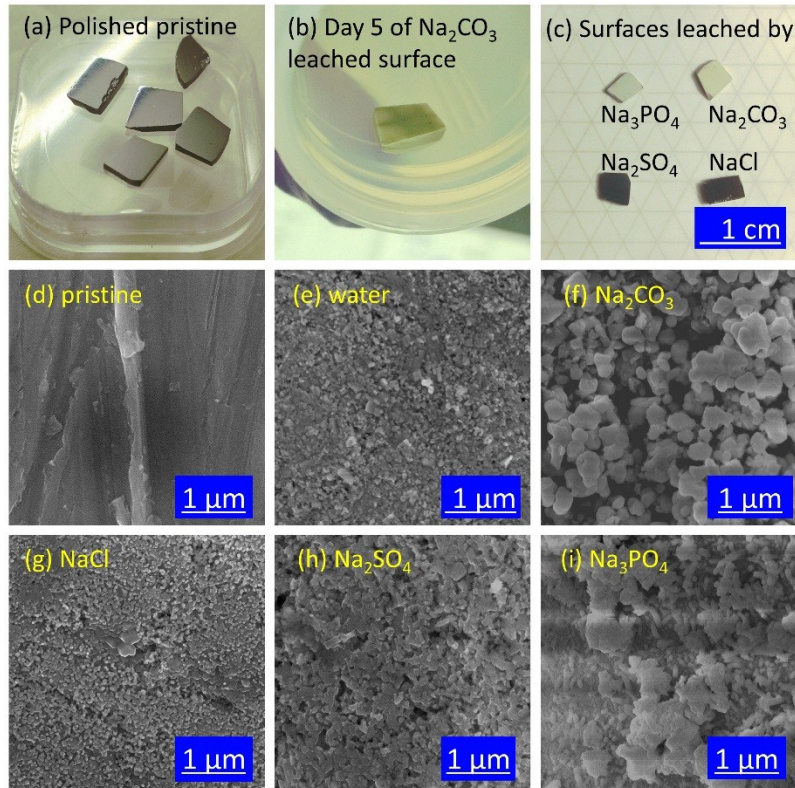
613

Graphical abstract



614

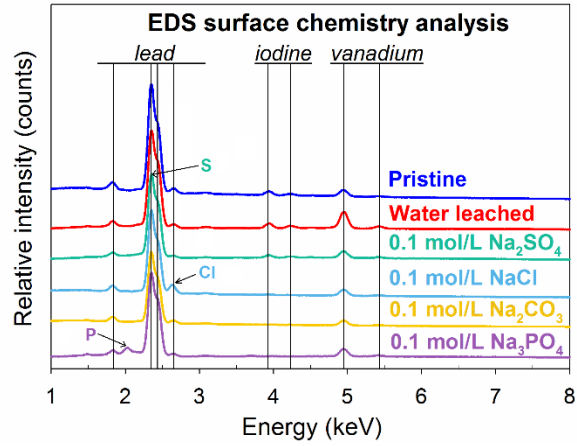
615



616

617 Fig. 1.(a) Polished pristine iodoapatite samples before test, (b) iodoapatite leached  
 618 surface during the 5<sup>th</sup> replacement of Na<sub>2</sub>CO<sub>3</sub> solution, (c) surface leached by at the end  
 619 of 14-day leaching tests, SEM images of (a) a polished pristine iodoapatite and the  
 620 samples leached by (b) deionized water, (c) 0.1 mol/L Na<sub>2</sub>CO<sub>3</sub>, (d) 0.1 mol/L NaCl, (e)  
 621 0.1 mol/L Na<sub>2</sub>SO<sub>4</sub>, and (f) 0.1 mol/L Na<sub>3</sub>PO<sub>4</sub>.

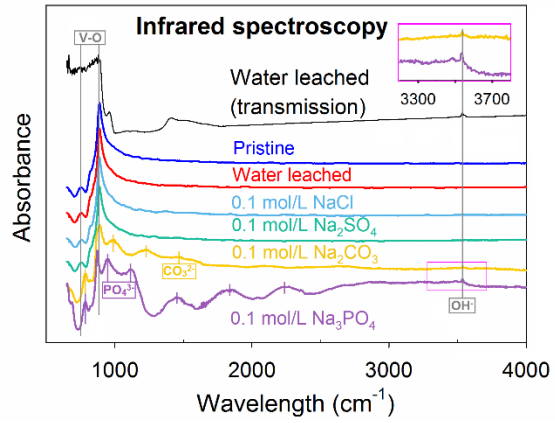
622



623

624 Fig. 2. EDS spectra of a pristine iodoapatite and the samples leached by deionized  
 625 water, 0.1 mol/L NaCl, 0.1 mol/L Na<sub>2</sub>CO<sub>3</sub>, 0.1 mol/L Na<sub>3</sub>PO<sub>4</sub>, and 0.1 mol/L Na<sub>2</sub>SO<sub>4</sub>  
 626 solutions.

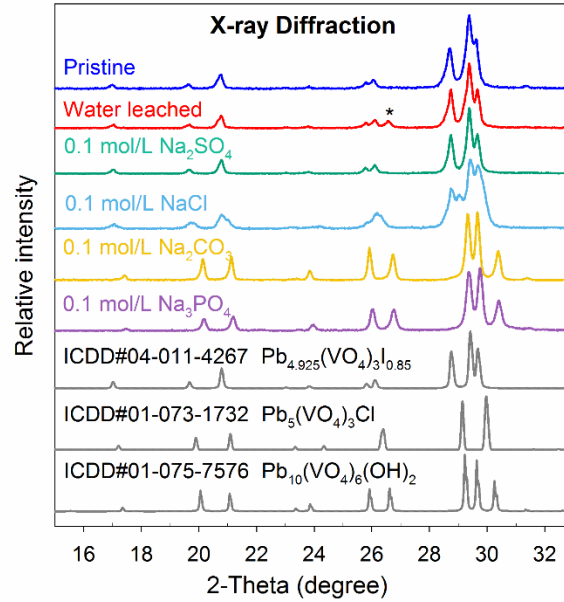
627



628

629 Fig. 3. Infrared spectroscopy of pristine iodoapatite and leached samples by deionized  
630 water, NaCl, Na<sub>2</sub>SO<sub>4</sub>, Na<sub>2</sub>CO<sub>3</sub>, and Na<sub>3</sub>PO<sub>4</sub> solutions.

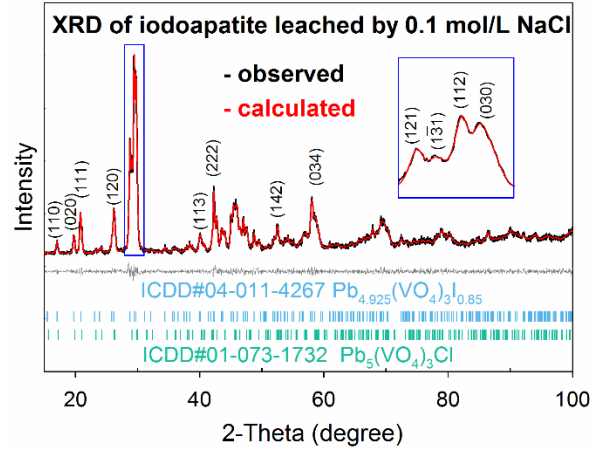
631



632

633 Fig. 4. XRD patterns of a pristine iodoapatite and the samples leached by deionized  
 634 water, 0.1 mol/L Na<sub>2</sub>SO<sub>4</sub>, 0.1 mol/L NaCl, 0.1 mol/L Na<sub>2</sub>CO<sub>3</sub>, and 0.1 mol/L Na<sub>3</sub>PO<sub>4</sub>. In  
 635 addition, standard XRD spectra of iodoapatite, vanadinite, and hydroxylvanadinite are  
 636 listed for comparison. \* denotes the graphite impurity introduced during sample  
 637 synthesis.<sup>25</sup>



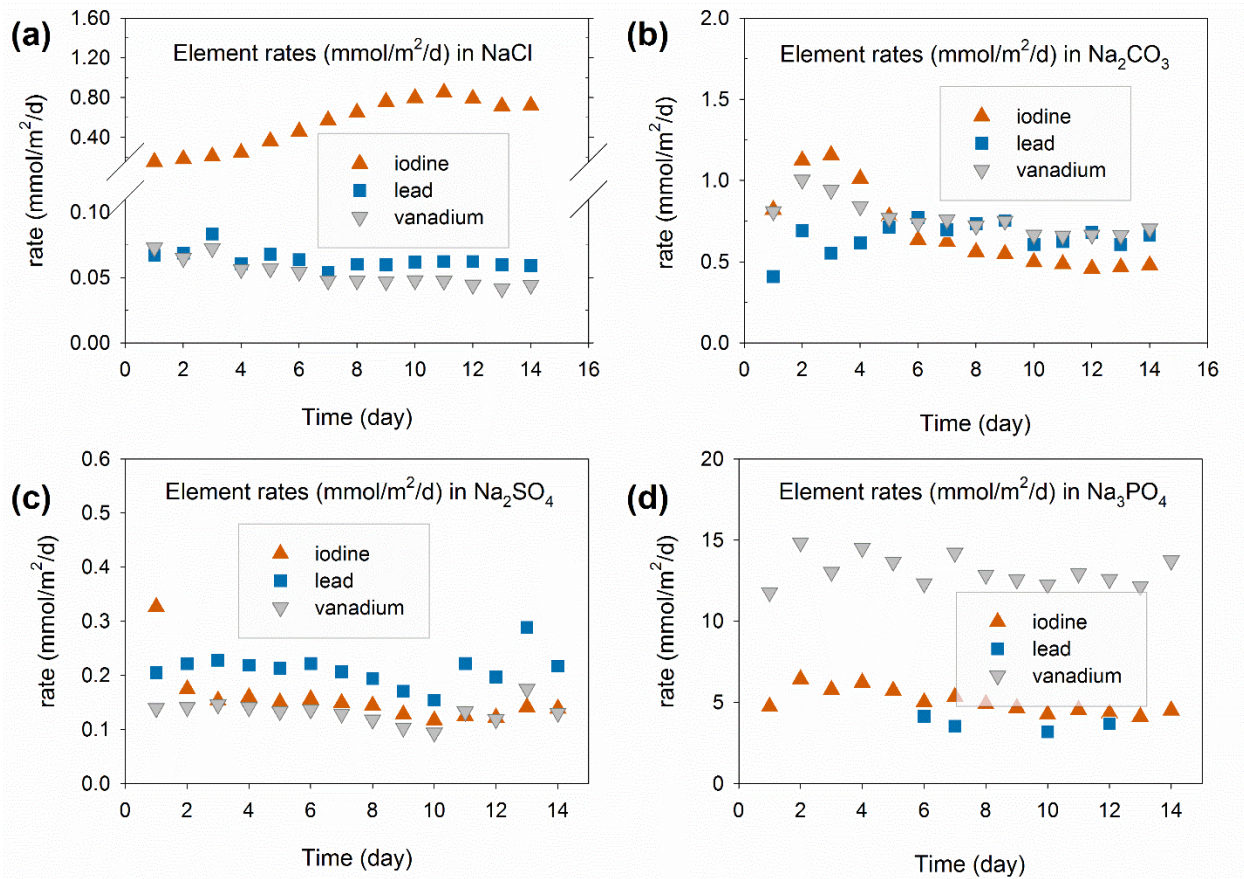


638

639 Fig. 5. XRD phase analysis of the iodoapatite sample surface leached by 0.1  
 640 mol/L NaCl solution. Two phases were identified: iodoapatite and vanadinite.

641

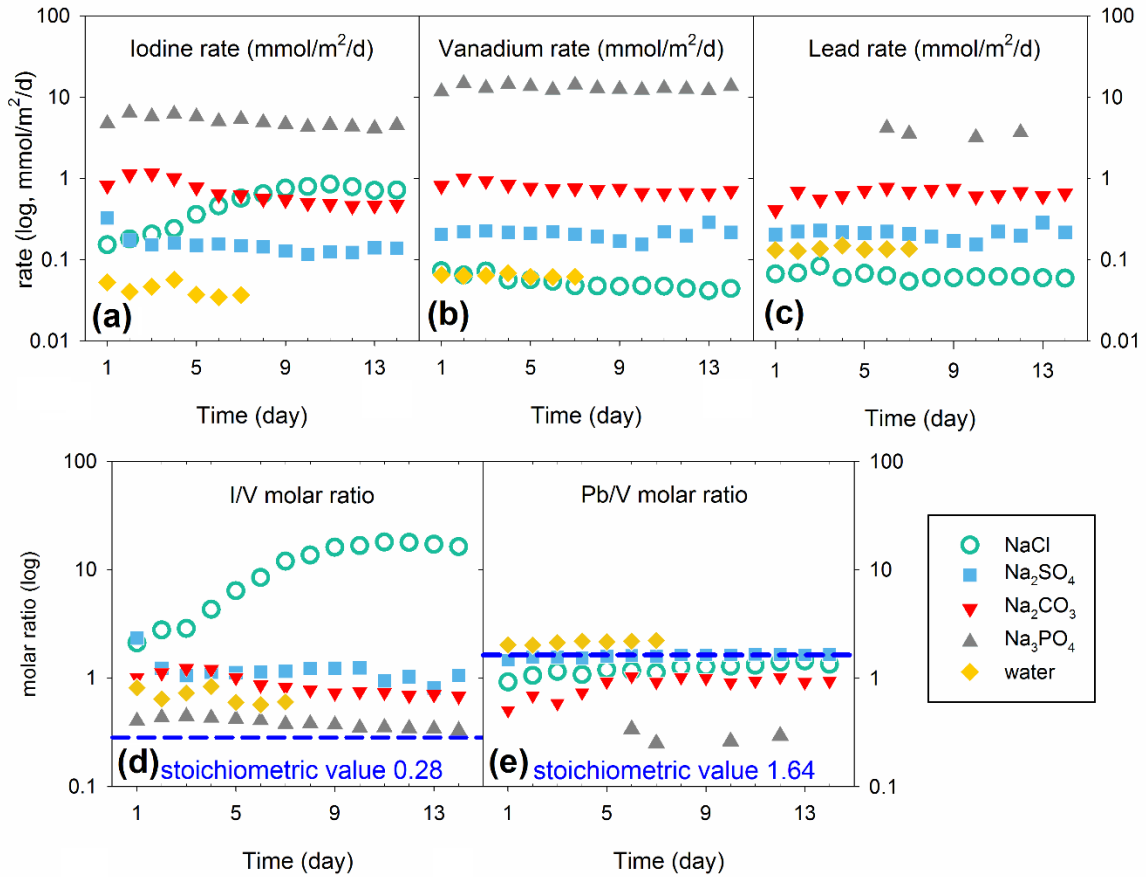
642



643

644 Fig. 6. Solution analysis of collected leachates from 14 days semi-dynamic leach tests  
645 on iodoapatite samples in (a) 0.1 mol/L NaCl, (b) 0.1 mol/L Na<sub>2</sub>CO<sub>3</sub>, (c) 0.1 mol/L  
646 Na<sub>2</sub>SO<sub>4</sub>, and (d) 0.1 mol/L Na<sub>3</sub>PO<sub>4</sub>.

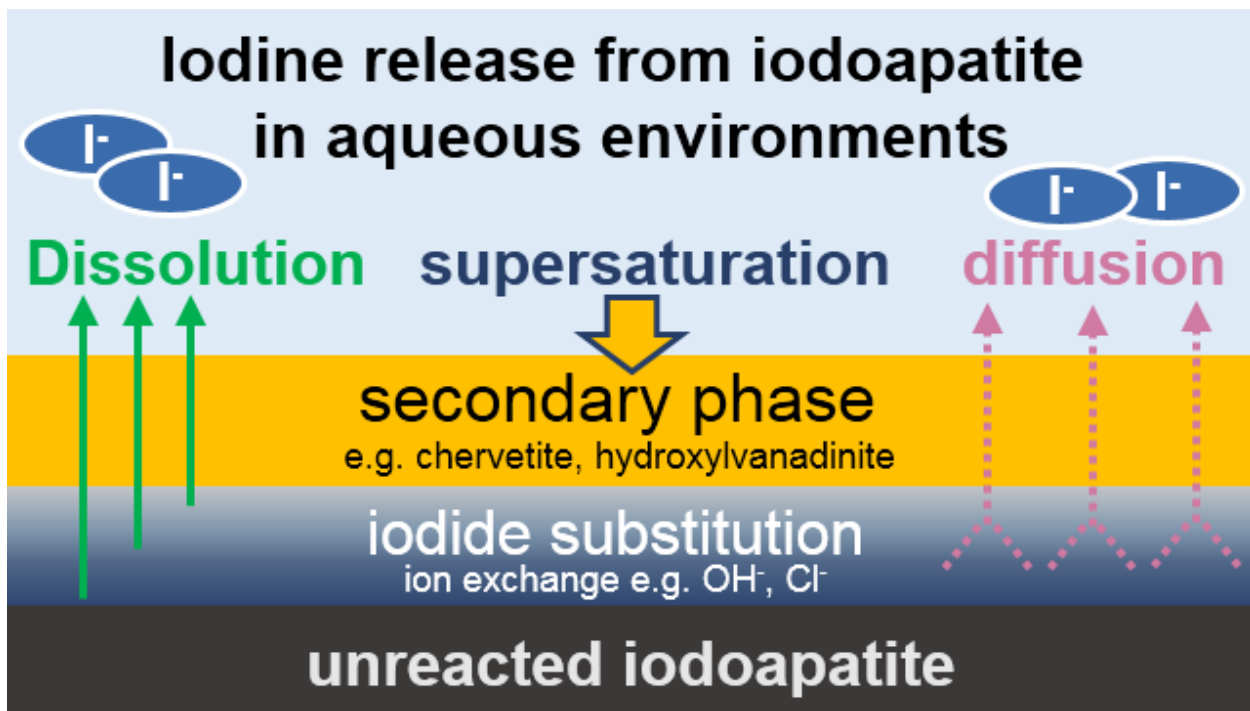
647



648

649 Fig. 7. Comparison of element release rate of iodine (a), vanadium (b), and lead (c) in  
 650 the leachate solutions from different leach tests. Molar ratios of Pb/V (d) and I/V (e) in  
 651 leachate solutions from leach tests in NaCl, Na<sub>2</sub>SO<sub>4</sub>, Na<sub>2</sub>CO<sub>3</sub>, Na<sub>3</sub>PO<sub>4</sub>, and deionized  
 652 water.

653



654

655 Fig. 8. Schematic diagram illustrates major processes that control the iodine release  
656 from iodoapatite in aqueous environments

657 Table. 1 Crystallographic parameters based on the XRD refinements by Le Bail  
 658 algorithm.

Leach test condition	Refined parameters				
	a, b (a=b, Å)	c (Å)	GoF	R <sub>p</sub> (%)	R <sub>wp</sub> (%)
Pristine	10.4420 (3)	7.4756 (3)	1.32	5.16	6.53
Water	10.4325 (3)	7.4864 (3)	1.63	6.04	7.73
0.1 mol/L Na <sub>2</sub> SO <sub>4</sub>	10.4336 (2)	7.4837 (2)	1.39	4.60	5.93
0.1 mol/L Na <sub>2</sub> CO <sub>3</sub>	10.1923 (2)	7.4656 (2)	1.65	4.85	6.44
0.1 mol/L Na <sub>3</sub> PO <sub>4</sub>	10.1984 (2)	7.4449 (2)	1.43	4.74	6.23
0.1 mol/L NaCl (2 phases)	10.4443 (6)	7.4796 (5)	1.17	4.12	5.28
	10.3536 (8)	7.3735(8)			
<b>Pb<sub>4.925</sub>(VO<sub>4</sub>)<sub>3</sub>l<sub>0.85</sub></b> [ICDD#04-011-4267]	10.422	7.467	<b>Crystal system:</b> hexagonal		
<b>Pb<sub>5</sub>(VO<sub>4</sub>)<sub>3</sub>(OH)</b> [ICDD#01-075-7576]	10.2242	7.4537	<b>Space group:</b> P63/m #176;		
<b>Pb<sub>5</sub>(VO<sub>4</sub>)<sub>3</sub>Cl</b> [ICDD#01-073-1732]	10.31	7.34	<b>α=90°</b> <b>β=90°</b> <b>γ=120°</b>		

659

660

661 Table 2. Solution chemistry at equilibrium state calculated by Visual MINTEQ under  
 662 90 °C.

mol/L 90 °C	Deionized water	0.1 mol/L NaCl	0.1 mol/L Na <sub>2</sub> SO <sub>4</sub>	0.1 mol/L Na <sub>2</sub> CO <sub>3</sub>	0.1 mol/L Na <sub>3</sub> PO <sub>4</sub>
pH (unitless)	6.1	6.1	6.2	10.3	10.9
Ionic strength	$2.04 \times 10^{-6}$	0.098	0.26	0.25	0.29
<b>Major cation</b>	<b>H<sup>+</sup></b>	<b>Na<sup>+</sup></b>	<b>Na<sup>+</sup></b>	<b>Na<sup>+</sup></b>	<b>Na<sup>+</sup></b>
Concentration	$6.52 \times 10^{-7}$	0.098	0.18	0.18	0.22
Activity	$6.51 \times 10^{-7}$	0.074	0.13	0.13	0.15
Activity coefficient	1.00	0.76	0.72	0.72	0.68
<b>Major anion</b>	<b>OH<sup>-</sup></b>	<b>Cl<sup>-</sup></b>	<b>SO<sub>4</sub><sup>2-</sup></b>	<b>CO<sub>3</sub><sup>2-</sup></b>	<b>PO<sub>4</sub><sup>3-</sup></b>
Concentration	$8.72 \times 10^{-7}$	0.098	0.079	0.069	0.012
Activity	$8.70 \times 10^{-7}$	0.074	0.02	0.017	0.00049
Activity coefficient	1.00	0.76	0.25	0.24	0.041

663